Chapter 9

Thermal, acoustic and seismic signals from pyroclastic density currents and Vulcanian explosions at Soufrière Hills Volcano, Montserrat

D. DELLE DONNE[1], M. RIPEPE[1]*, S. DE ANGELIS[2], P. D. COLE[3,4], G. LACANNA[1], P. POGGI[5] & R. STEWART[4]

[1]*Dipartimento Scienze della Terra, Universita' di Firenze, via G. La Pira, 4, 50121 Firenze, Italy*

[2]*School of Ocean and Environmental Sciences, Department of Geology and Geophysics, University of Liverpool, 4 Brownlow Street, Liverpool L69 3GP, UK*

[3]*Montserrat Volcano Observatory, Flemmings, Montserrat, West Indies*

[4]*Seismic Research Centre, The University of the West Indies, St Augustine, Trinidad & Tobago, West Indies*

[5]*INO (Istituto Nazionale di Ottica), Largo E. Fermi, 6, 50125 Firenze, Italy*

**Corresponding author (e-mail: maurizio.ripepe@unifi.it)*

Abstract: We show two examples of how integrated analysis of thermal and infrasound signal can be used to obtain, in real time, information on volcanic activity. Soufrière Hills Volcano (SHV) on Montserrat offers the opportunity to study a large variety of processes related to lava-dome activity, such as pyroclastic density currents (PDCs) and large Vulcanian eruptions. Infrasound and thermal analysis are used to constrain the propagation of PDCs and their velocities, which are calculated here to range between 15 and 75 m s^{-1}. During the Vulcanian eruption of 5 February 2010, infrasound and thermal records allow us to identify an approximately 13 s seismic precursor possibly related to the pressurization of the conduit before the explosion onset. The associated very long period (VLP) seismic signal is correlated with the gas-thrust phase detected by thermal imagery, and may reflect a change in the upward momentum induced by the mass discharge. Moreover, from infrasound and thermal analysis, we estimate a gas-thrust phase lasting 22 s, with an initial plume velocity of approximately 170 m s^{-1} and a mean volumetric discharge rate of 0.3×10^5–9.2×10^5 m^3 s^{-1}. This information provided in real time gives important input parameters for modelling the tephra dispersal into the atmosphere.

Lava dome eruptions represent a style of volcanism of distinctive interest because of their potential consequences, such as the generation of pyroclastic density currents (PDCs) down the volcano's flanks and large explosive eruptions following partial-dome collapse. Lava domes are formed by silica-rich lava that is too viscous to flow and, instead, builds-up over the point of extrusion. The hazards from lava-dome eruptions are well known owing to unpredictable transitions from the slow extrusion of viscous lava to vigorous explosions, and to the propensity of lava domes to suddenly collapse, spawning devastating PDCs down the flanks of volcanic edifices (Young *et al.* 1998; Sparks & Young 2002). As a lava dome grows, parts of it may collapse because of gravitational instability or as the result of gas explosions within the dome itself, thus forming PDCs. The ability to detect and track the propagation of these fast-moving density currents is of utmost importance in understanding the evolution of lava dome eruptions and mitigating related hazards.

Methods for the location of PDCs, based on seismic amplitudes, have been proposed in the past (e.g. Jolly *et al.* 2002) and have proved quite effective for the characterization of large collapse events. These techniques require dense seismic networks and optimal azimuthal coverage; both conditions are rarely met on lava dome volcanoes where seismic networks are sparse because of the restrictions imposed by rough terrain and eruption hazards. The use of seismic amplitudes requires understanding of local site effects and frequency-dependent attenuation, thus introducing another layer of complexity. Finally, these methods are not designed for unsupervised application in real-time; events classification and location require visual inspection of the seismograms, and manual intervention of a seismic analyst.

Ripepe *et al.* (2009) recently demonstrated the use of infrasound array technology to detect and track the evolution of PDC activity in real time. In this chapter we extend their work by introducing methods based on the integrated analyses of thermal imagery and infrasound array data to evaluate, with unprecedented resolution, the propagation velocity of PDCs. We show our results are in good agreement with predictions from theoretical models.

We use a thermo-acoustic method to constrain the duration of the gas-thrust phase, and the plume exit velocities at the vent during a Vulcanian eruption. Here we show how the integrated infrasound and thermal analysis for a large Vulcanian eruption that occurred at Soufrière Hills Volcano (SHV) on 5 February 2010 helps to better understand the associated seismic signal. Our aim is also to give an estimate of the plume exit velocity and volume flux that are important input parameters for the tephra dispersal predictive models evaluating the amount of volcanic ash emitted into the atmosphere.

Thermal camera and infrasonic array at MVO

A thermal camera and an infrasound array (Fig. 9.1) were colocated at Montserrat Volcano Observatory (MVO) at a distance of approximately 5.6 km from SHV. The camera is a FLIR A20 model, and is equipped with $34^\circ \times 25^\circ$ optical lens of 9.2 mm and a maximum thermal resolution of 0.1 °C in the 7.5–13 μm wavelength interval. The camera field of view (FOV) above SHV is approximately 3.5×2.5 km, and it allows monitoring of both PDC activity towards the west (Plymouth), the NE (Old Airport) and to the north (Tyre's Ghaut and Belham Valley) as well as the explosive activity (Fig. 9.1). The thermal image acquisition and processing system has been designed to fulfil the specific needs of the MVO personnel, and is able to process, in real time, the large 352×244 pixel thermal images at two frames per second. A global positioning system (GPS) time-stamp on each frame allows synchronization with all other sensors

From: Wadge, G., Robertson, R. E. A. & Voight, B. (eds) 2014. *The Eruption of Soufrière Hills Volcano, Montserrat from 2000 to 2010.* Geological Society, London, Memoirs, **39**, 169–178. http://dx.doi.org/10.1144/M39.9

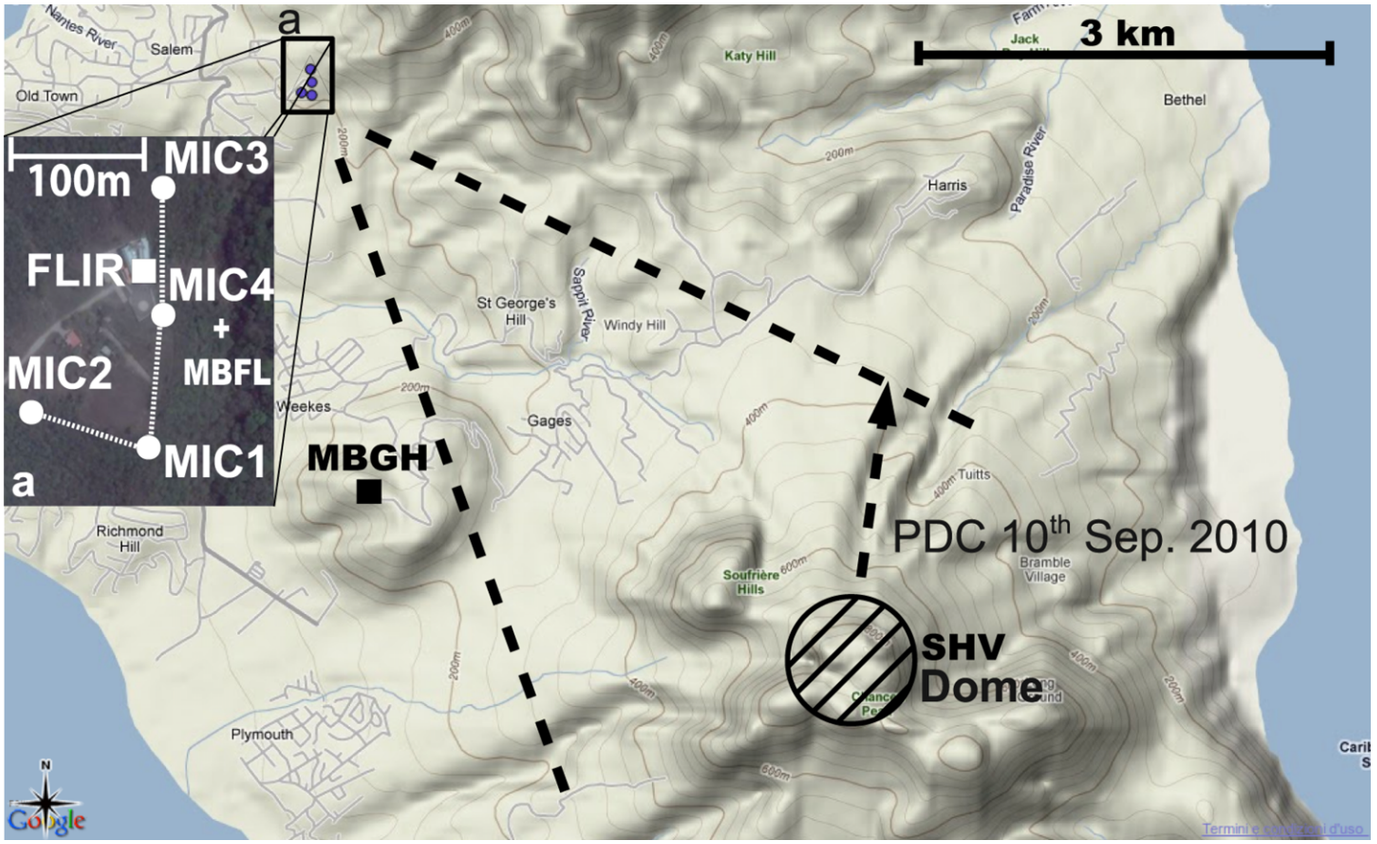

Fig. 9.1. Map with the position of the infrasonic array (MIC1, MIC2, MIC3 and MIC4), thermal camera (FLIR) and seismic-acoustic stations (MBFL and MBGH). The FOV of the thermal camera and the trajectory of the 10 September 2010 PDC are also shown with dashed lines.

recorded by the MVO seismic network (Luckett *et al.* 2007). This allows successful integration of thermal camera information within the MVO monitoring network, thus assisting observatory staff with decision making during volcanic crises. This could include providing advice to local authorities about the ongoing eruptive activity, and prompting the evacuation of local population from areas potentially at risk from PDCs.

Volcanic activity is also monitored by an infrasonic array installed close to the MVO (Fig. 9.1) and at the same distance, approximately 5600 m, from the SHV lava dome. The array has a four-element 'L' geometry, with a total aperture of 220 m. Each element of the array is equipped with 'Item-prs' differential pressure transducers, with a sensitivity of 25 mV Pa^{-1}, 250 Pa of full-scale range, a flat instrument response in the frequency band of 0.01–100 Hz, and a noise level of 10^{-2} Pa. The infrasonic signals are digitized with a resolution of 16 bits at 50 Hz sampling rate. The satellite sensors are connected to the receiver unit by fibre-optic cables. The use of fibre-optic technology provides an optimal signal-to-noise ratio (SNR), and protects the network from lightning hazards. Data are sent via RS-232 to the MVO where they are also processed in real time, archived and broadcast via the Internet (Ripepe *et al.* 2010).

Thermal image processing

Thermal imagery is processed measuring both the propagation vector field of PDCs and the upwards velocities of the tephra-plume. This is accomplished by: (1) converting thermal pixels to metres; (2) back-projecting pixels to the topography using a digital elevation model (DEM); and (3) tracking the vertical and horizontal propagation of the thermal anomalies associated with PDCs and volcanic plumes in successive frames.

The processing used is based on the thermal analysis method of single images. This method analyses the propagation front at different temperature levels (Marchetti *et al.* 2009; Pistolesi *et al.* 2011; Delle Donne & Ripepe 2012). In summary, thermal images, $I_t(t, x, y)$ are converted into binary images, $I_b(t, x, y)$ (Fig. 9.2) according to the following formulae:

$$I_b(t,x,y)\begin{cases} 1, I_t(t,x,y) > T_{bkg} \\ 0, I_t(t,x,y) \le T_{bkg} \end{cases}, \tag{1}$$

where T_{bkg} is the ambient background temperature. Thus, for each frame $I_t(t)$ we obtain the distribution (x, y) of pixels characterized by temperatures higher than the background T_{bkg} and consider that they are related to volcanic material (e.g. pyroclasts, juvenile ash). It is worth noting that the temperatures given by thermal images are apparent because the cores of PDCs or volcanic plumes can be masked by the cloud exterior. We then estimate the high-temperature pixel distribution in the vertical, V_d, and horizontal, H_d, axis by adding up all the pixels, I_b, along the same row and for each column of the image (Fig. 9.2):

$$\begin{aligned} V_d(t,x) &= \sum_{y=1}^{y=Y} I_b(t,x,y) \\ H_d(t,y) &= \sum_{x=1}^{x=X} I_b(t,x,y), \end{aligned} \tag{2}$$

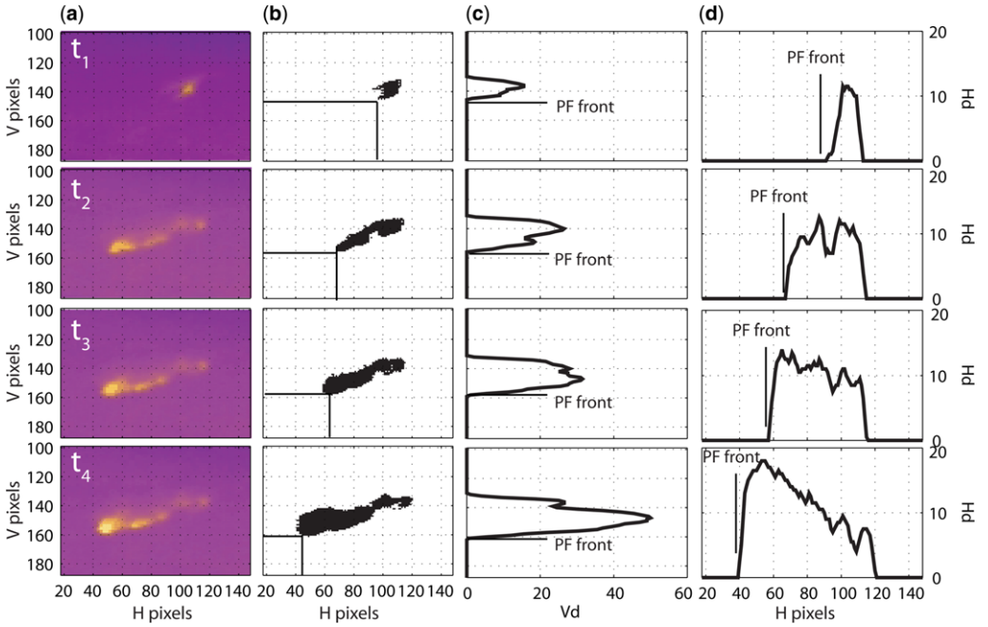

Fig. 9.2. PDC tracking methodology. (**a**) Original thermal images captured at the t_1–t_4 time interval are converted into (**b**) binary images using a background temperature threshold and allowing us to detect high-temperature areas in the FOV. Image decomposition method along (**c**) vertical and (**d**) horizontal axes allows tracking of the front of the high-temperature anomaly.

where X and Y are the horizontal (352 pixels) and the vertical (244 pixels) size of the image, respectively. $V_d(t, x)$ and $H_d(t, y)$ are the distribution functions representing the number of pixels with temperature above T_{bkg} along every horizontal and vertical line in the FOV, and thus represent the extension of the high-temperature areas in the two directions. This analysis enables tracking the front of the thermal anomaly in the vertical and horizontal directions by picking the pixel coordinates where the distribution functions $V_d(t, x)$ and $H_d(t, y)$ increase (Fig. 9.2). Combining the information from the vertical and horizontal components, it is possible to calculate the apparent trajectory of the thermal anomaly (Fig. 9.2).

In order to calculate the propagation velocity of the thermal front, we convert pixel coordinates into metres by georeferencing the thermal images using five reference points with known geographical coordinates that are present and easily recognizable in the thermal image. We use the 'Thin plate smoothing spline' interpolation algorithm (Bookstein 1989) in order to produce a new 'warped' georeferenced image linked to the five reference points (Fig. 9.3). This georeferencing procedure is known as the non-rigid transformation model. Error in the warping method is not constant over the entire image, but depends on the distance from the reference points. Assuming that close to the reference points the error is small, to minimize the warping error, reference points have been selected over most of the image and as close as possible to the PDCs area. However, the topography around the dome changes rapidly with time and a reliable DEM is not always available. For this reason the velocities derived by our thermal imagery should not to be considered as absolute velocities but rather as indicative of the mean velocity of the PDC front. The error in the velocity estimates depends on the pixel size of the thermal images (*c.* 10 m at a distance of 5600 m from the vent) and frame rate (2 Hz = 0.5 s). As a result, the instantaneous velocity has a maximum error of $\pm 10\ \mathrm{m\ s^{-1}}$. Figure 9.3 shows how the georeferenced thermal images appear once they have been projected onto Google Earth by using the default 3 arcsecond (3′) (*c.* 100 m) DEM available on Google Earth software. This procedure permits projection of two-dimensional (2D) thermal images onto 3D topography to precisely locate the position of the thermal front draped on topography. This is an extremely useful tool if integrated into the monitoring and alert system because it permits real-time location of the extension and propagation of the PDCs.

Infrasound array processing

During explosions, such as those that have occurred at SHV, infrasound is produced by volumetric sources rapidly expanding into the atmosphere, but it is also formed by non-explosive sources related to dome collapses, such as PDCs, rockfalls and lahars.

The permanent small-aperture (220 m) four-element infrasonic array, such as that deployed at the MVO, has proved its ability to detect both point sources, such as explosive events, and non-point moving sources, such as PDCs and debris flows, in real-time (Ripepe *et al.* 2010). Source location is based on the assumption that a signal is coherent at the different sensors, whereas noise is not correlated. The array processing applies multichannel correlation using a grid-searching method to identify signals from noise in terms of wave propagation back-azimuth and apparent velocity. The propagation back-azimuth indicates the direction of the signal source. Assuming that infrasound reaches the array as a planar wave front, with 90° incident angle (from the vertical) at constant velocity, infrasonic waves should propagate across the array at the same speed of sound (*c.* 340 m s^{-1}), which depends primarily on air temperature and, to a small extent, on humidity. This assumption of plane-wave propagation is justified as the source–receiver distance of approximately 5600 m is considerably larger than the 220 m aperture of the array.

The apparent velocity is the velocity that the wave will have when it is not travelling in the same plane as defined by the array; that is with an incident angle $<90°$. High apparent velocities ($>340\ \mathrm{m\ s^{-1}}$) will thus be related to lower incident angles ($<90°$) and, therefore, to a source located above the array plane. It is worth noting that the maximum difference in elevation between sensors is 30 m over 220 m of aperture, so that the ideal plane defined by the array is very close to the horizontal. Variation in apparent velocity will indicate a change in the altitude and, hence, a moving source. Furthermore, high apparent velocities ($>400\ \mathrm{m\ s^{-1}}$) correspond to steep incident angles that represent unrealistic sources originating from the volcano.

The degree of signal correlation across the array is controlled by the time residual. The time residual is the sum of the delays between three array sensor pairs calculated in real time by multiple cross-correlation. Highly correlated signals (>0.8) have a time residual approaching 0. This procedure (see Ulivieri *et al.* 2011

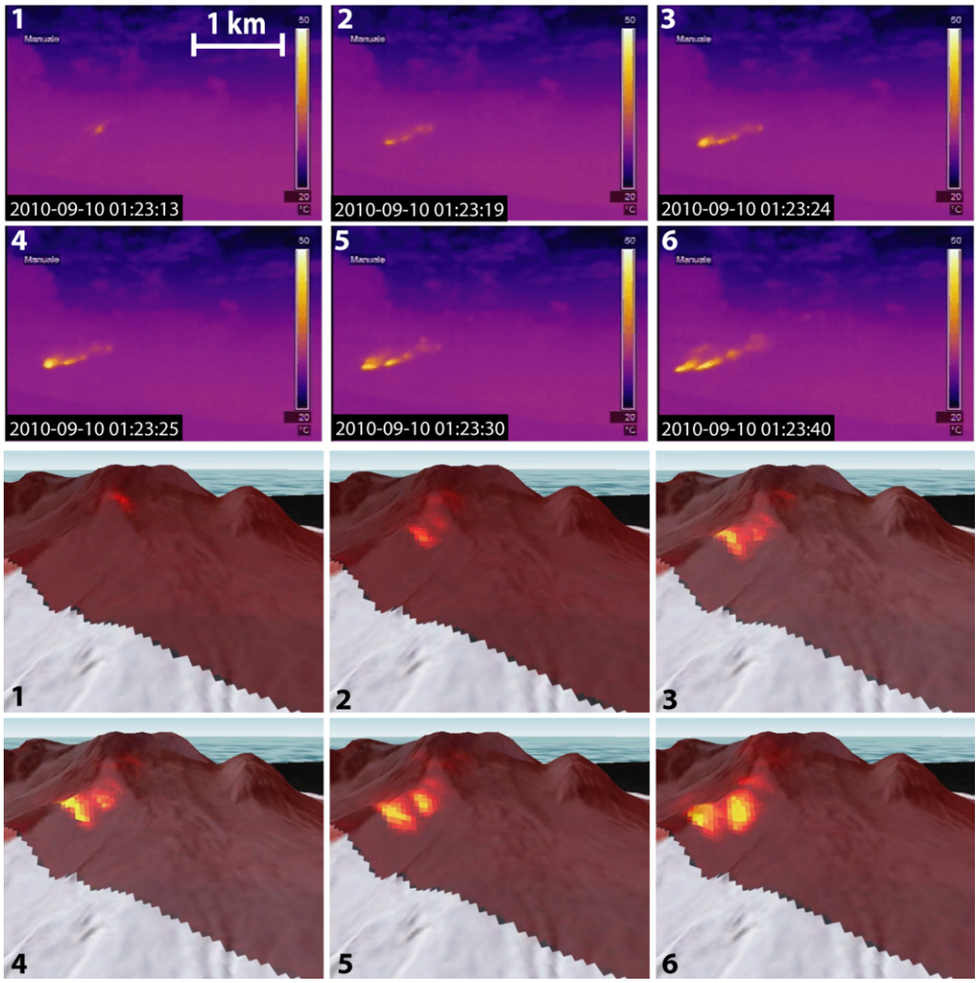

Fig. 9.3. Six snapshots associated with the PDC that occurred on 10 September 2010 and running towards the NE along the collapse scar produced by the 11 February 2010 partial dome collapse, as detected by the FLIR thermal camera (top two rows) and associated 3D Google Earth view (bottom two rows) after thin plate smoothing spline georeferencing.

among others) is performed for all the possible triplets of sensors of the array, and we consider a detection to be valid if the mean of time residuals is below the consistency threshold of 0.015 s, which corresponds to a 70% correlation for a signal with a peak frequency of 1 Hz. The propagation back-azimuth and apparent velocity is calculated as the mean value between all the possible combination of sensors within the different triplets using the distances and the time delays, and assuming a constant propagation velocity (see Cansi 1995; Ulivieri *et al.* 2011 for details). The accuracy of the array back-azimuth depends on the array aperture, sampling rate, frequency content of the infrasonic signal and the SNR. For a 220 m aperture array and considering a frequency content of 1 Hz, typical of infrasound generated by volcanic activity, the expected azimuth resolution is approximately 0.9°, which corresponds to 88 m at 5600 m of slant distance.

The use of a small-aperture infrasonic array improves the capabilities of volcano observatories for monitoring activities during eruption crises (e.g. Ripepe *et al.* 2007; Johnson & Ripepe 2011), and also provides useful corroboration for other geophysical parameters (mainly seismic signals, ground visible and thermal cameras, and gas monitoring) (Garces *et al.* 2000; Vergniolle & Caplan-Auerbach 2006; Johnson 2007).

This location procedure is performed in real time using 5 s moving windows with 90% overlap on all possible triplets of sensors in the array, and allows detection and tracking of infrasound generated by PDCs. Once a coherent arrival across the array is detected, we use back-azimuth and incident angle information to map the source onto the DEM.

Thermo-acoustic tracking of the propagation of PDCs

The propagation of the PDCs is mainly controlled by three parameters: topography, basal friction angle (an empirical property of two contacting materials) and initial velocity. While the topography is well known, and the basal friction angle can be estimated to be of the order of 12–16.5° (Nikolkina *et al.* 2011), data of initial velocities of the PDCs from the SHV are poorly documented. Average velocities of propagation have been measured in the range of 5–35 m s^{-1} (Calder *et al.* 2002; Cole *et al.* 2002; Carn *et al.* 2004), but modelling suggests that initial velocities of dome-collapse-induced PDCs can be much higher, reaching approximately 50–70 m s^{-1} (Wadge *et al.* 1998; Calder *et al.* 1999; Hooper & Mattioli 2001). The estimation of propagation velocity of PDCs is crucial to estimating hazards as velocity controls the run-out and the extents of the affected area of the PDC.

The combined thermal and infrasonic methods previously described are used here to analyse the kinematics of a PDC formed on 10 September 2010 by gravitational instability of the remaining lava dome at SHV. The source of the PDC was on the western side of the headwall of the amphitheatre-shaped scar, formed by the partial dome collapse on 11 February 2010. PDCs are routinely detected by the thermal camera and are easily recognized in the imagery because of their higher temperature with respect to the background level (Fig. 9.3). The method of image decomposition is applied to track the propagation fronts of the PDC (Fig. 9.2), and to estimate displacement vectors in both the horizontal and vertical component. Once the image pixels are converted to metres, we may calculate the apparent movement of

the PDC front, which in this case is 960 m in the horizontal direction and 280 m in the vertical over 38 s (Fig. 9.4). Thus, we calculate the mean absolute apparent velocity of propagation as 26 m s^{-1}. Thermal image processing indicates a peak flow velocity of about 65 m s^{-1} at the onset of the PDC (Fig. 9.5a). Over the following 15 s the PDC showed a rapid deceleration down to a constant value of about 20 m s^{-1}. During the successive 20 s, the PDC moved downhill at an almost constant velocity of around 20 m s^{-1} (Fig. 9.5a). The transition between the rapid deceleration and the constant velocity regimes is marked by a change of slope in the topography (Fig. 9.5d), and thus suggests a topographical control on the PDC dynamics.

These thermally derived PDC peak and mean velocities are consistent with previous estimates (Wadge *et al.* 1998; Calder *et al.* 1999; Hooper & Mattioli 2001; Formenti *et al.* 2003; Ripepe *et al.* 2010).

Thermal images for the same PDC show a second moving front in the horizontal and vertical directions (frames 3–6 of Fig. 9.3). In particular, for the PDC in Figure 9.3, thermal images show at 01:23:24 (frame 3) a NE-flowing high-temperature anomaly that is related to a second PDC following the main thermal front that occurred at 01:23:13. For this second PDC, the thermal camera detected displacement of 420 m in the horizontal and 100 m in the vertical directions, giving a total of approximately 432 m of displacement in 25 s (from 01:23:24 to 01:23:49) and an average velocity of around 17 m s^{-1} (Figs 9.4 & 9.5).

Infrasonic waves in the 0.7–3 Hz frequency range related to PDCs have been previously measured on Unzen and SHV volcanoes (Yamasato 1997; Oshima & Maekawa 2001; Ripepe *et al.* 2010), and have been explained as being produced by the displacement of the atmosphere caused by the migration of the PDC front down the volcano's flank. The infrasound signal associated with the 10 September 2010 PDC event shows an emergent signal with peak amplitude of about 1 Pa at 5600 m from the source (Fig. 9.5e). Array processing shows coherent arrivals lasting for 28 s (Fig. 9.5c), with a shift in the first event's back-azimuth from 142°N to 130°N occurring in 11.4 s, from 01:23:28 to 01:23:39. At a slant distance of 5600 m, this back-azimuth shift towards the NE corresponds to a distance of 855 m, giving an apparent velocity of around 75 m s^{-1}. Considering a back-azimuth resolution of 0.9° that corresponds to 88 m at the dome, we can estimate an error in the velocity estimates of less than ±8%.

Following this, the infrasonic back-azimuth jumps back to 139°N and then shifts again toward the NE to 130°N in 10.4 s. This second shift in the back-azimuth indicates that a second PDC was generated that moved at an apparent velocity of about 55 m s^{-1}. After that, the back-azimuth remains almost constant, ranging between 128°N and 134°N around an average direction of 131°N. This direction does not coincide with the dome but seems more associated with the change in the slope of the topographical profile (Fig. 9.5b, d), suggesting that infrasound could be generated by the deceleration of the flow as it moved downhill. If we consider that the total shift of the infrasonic back-azimuth from 142°N to 128°N corresponds to a movement of 980 m over 28 s, then this is consistent with a downhill propagation of the PDC at a mean velocity of approximately 35 m s^{-1}.

Infrasound and thermal image analysis are consistent with PDC dynamics characterized by two propagation fronts moving toward the NE at a mean velocity ranging between 20 and 35 m s^{-1}, and with a peak initial down-slope velocity of 55–75 m s^{-1} (Fig. 9.5a, c).

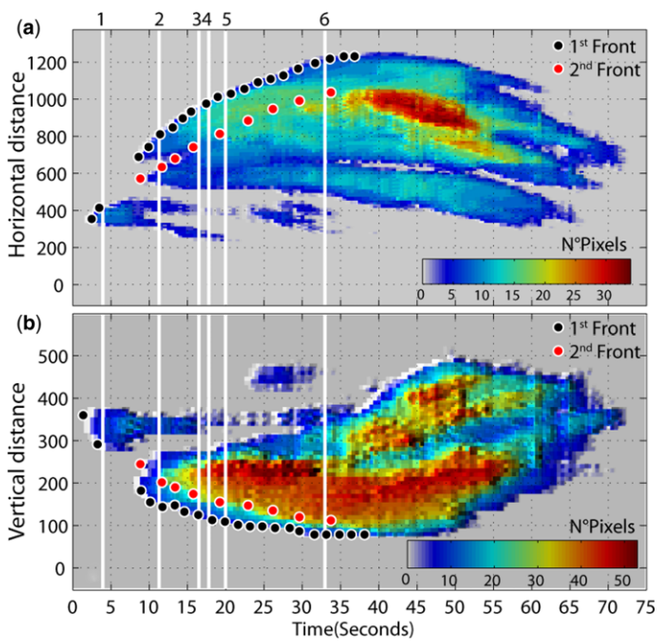

Fig. 9.4. Temperature distribution along (**a**) the horizontal (H_d) and (**b**) the vertical (V_d) thermal image axes plotted as a function of time. This analysis allows tracking of the thermal fronts (black dots) along the vertical and the horizontal directions, and the calculation of their propagation velocities. White vertical lines with the associated numbering refer to the thermal snapshots shown in Figure 9.3.

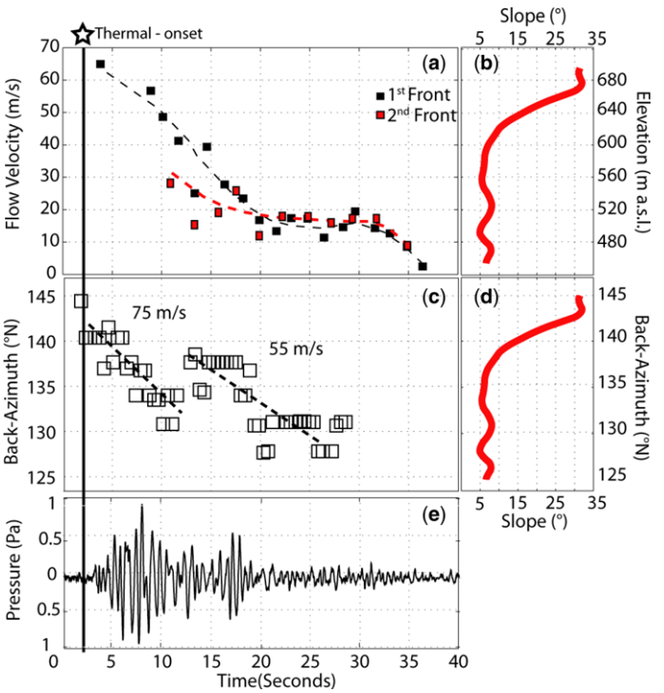

Fig. 9.5. (**a**) Thermal-derived velocity time-history of the two PDCs detected in the thermal images of Figure 9.3 are compared to (**c**) the infrasonic back-azimuth of (**e**) the associated infrasonic record. Thermal and acoustic analyses are both indicating a source that is moving from the dome to the NE with initial velocities of between 65 and 75 m s^{-1}. This velocity decreases after about 900 m (back-azimuth 131°N) from the dome down to approximately 20 m s^{-1}, which coincides with the slope changes in the topography and a stable infrasonic back-azimuth (**b** & **d**).

Thermal and acoustic observation of a Vulcanian explosion

Combined analysis of acoustic and thermal images can also provide valuable information on the dynamics of eruptive

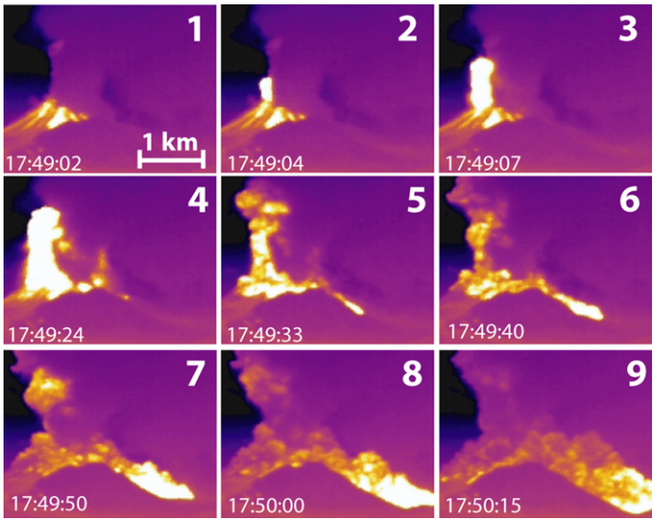

Fig. 9.6. Thermal snapshots related to the Vulcanian eruption that occurred on 5 February 2010. The thermal gas-thrust phase is represented in the frames 1–4, after which the volcanic plume starts to collapse, generating large PDCs.

columns (Yokoo & Iguchi 2010; Delle Donne & Ripepe 2012). Both techniques can be used to constrain the eruptive onset, plume exit velocity and volumetric flux. Furthermore, the correlation of infrasound with thermal imagery can provide an important contribution to interpreting the associated seismic activity. Here we present the results of real-time processing of infrasound and thermal data associated with a Vulcanian explosion occurring at 17:49 UTC on 5 February 2010 (Fig. 9.6). The seismic signal associated with this event lasted approximately 7 min, sending a tephra column to an elevation of 7.3 km above sea level (asl) into the atmosphere (Cole *et al.* 2014). Direct observations showed extensive ballistic fragments showering the northern and western flanks of the volcano up to distances of around 1 km. The vent area of the explosion was the western side of the lava-dome summit. The largest PDC associated with this explosion reached the sea (run-out of >4 km) at Aymers Ghaut, and minor PDC activity (run-out of <2 km) also occurred in several other valleys, including Tyre's Ghaut (Cole *et al.* 2014).

Thermal image analysis

The thermal camera imagery captured the main phases of the explosion dynamics (Fig. 9.6), with the initial injection of tephra into the atmosphere (frames 1–4) at 17:49:02, followed by plume collapse at 17:49:36 (frames 4–9). It is of note that within about 22 s of the onset (frame 4) the thermal camera shows a decrease in the integrated temperature in the FOV, indicating that the tephra-column cooling related to a convective air entrainment mechanism and/or to an increase of cold ash in the atmosphere, which was preventing the detection of the volcanic activity at the dome.

Explosive eruptions are generally described by two main gas dynamic phases. During the first phase, the volcanic plume is driven into the atmosphere by the gas thrust. Following this, the plume keeps rising at a relatively constant velocity by buoyancy, slowly expanding into the atmosphere while entraining air (Wilson 1980; Patrick 2007). The gas-thrust phase feeds hot tephra into the plume and is responsible for the increase in the temperature within the thermal camera FOV. The buoyancy phase is, however, associated with the reduction in the temperature in the FOV as no new volcanic material is ejected, but, rather, the plume rises at constant velocity by convective air entrainment with a consequent reduction of its internal temperature (Wilson 1980; Patrick 2007; Marchetti *et al.* 2009; Delle Donne & Ripepe 2012).

Thermal analysis provides the vertical rise velocity of the eruptive plume front, and the time-history of the plume-integrated temperature (Fig. 9.7e, f). This analysis shows that this Vulcanian explosion is characterized by the ejection of gas and fragments into the atmosphere with initial velocities of about 170 m s^{-1}, which is followed by a sharp deceleration phase lasting approximately 13 s. The plume velocity becomes nearly constant at around 27 m s^{-1}, during which the gas thrust is still feeding the plume for about other 9 s, as also evidenced by the progressive increase of the integrated temperature (Fig. 9.7e, f, grey marked phase) for a total duration of 22 s. These plume velocities are fully consistent with previous estimates of 40–140 m s^{-1} using image analysis of

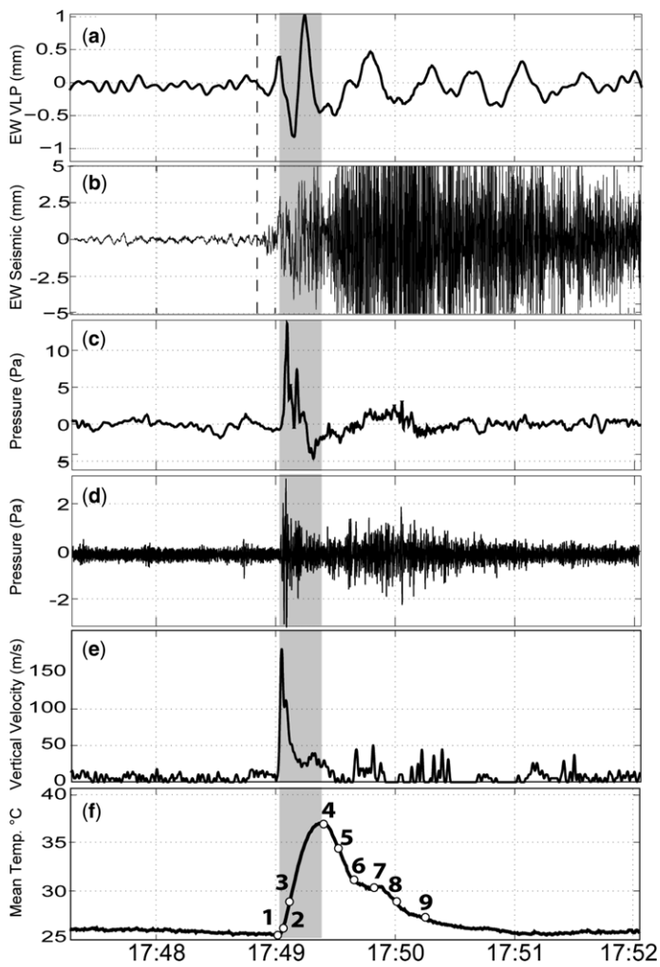

Fig. 9.7. Seismic-, acoustic- and thermal-derived signals associated with the 5 February 2010 Vulcanian eruption. (**a**) Seismic VLP ground displacement (using non-causal filter of Fig. 9.8) associated with the eruption onset. This signal is not evident but is still visible in the raw data (**b**), which has a strong high-frequency (1–20 Hz) amplitude component. Seismic onset is highlighted by the dashed black line and preceding the explosion (thermal and infrasound) onset by 13 s. Infrasound filtered between 0.2 and 20 Hz (**d**) indicates a high-frequency cigar-shape signal associated with PDC activity induced by the plume collapse that is correlated with the high-frequency seismic signal (b). Unfiltered infrasound (**c**) and thermal camera image processing (e, plume velocity; f, mean temperature) detected the eruption onset at 17:49:02, which was characterized by an exit velocity of 170 m s^{-1} (**e**) and a sharp positive compressive acoustic signal (c). Temperature (**f**) above the vent increased for approximately 13 s (point 4) in agreement with the duration of the seismic VLP (a), infrasonic broadband compression (c) and plume velocity (e). We suggest this is the duration of the eruptive gas-thrust phase (grey area) followed by the plume collapse and the generation of the PDCs.

video camera records for several Vulcanian explosions occurring at SHV during the 1997 eruptive sequence (Druitt *et al.* 2002; Formenti *et al.* 2003).

At the end of the gas-thrust phase, the eruptive dynamics are marked by the collapse of the plume that generates impressive PDCs (frames 4–9 in Fig. 9.6), which reached the sea with a run-out of >4 km. We interpret this collapse as being responsible for the decrease in the integrated temperature in the thermal trace (Fig. 9.7).

Infrasonic and seismic records

This Vulcanian explosion was recorded both with the MVO broadband seismic network and with the infrasonic sensor at the MBFL station at the MVO (Fig. 9.8). The seismic signal shows a main duration of about 7 min (Fig. 9.8a), which includes both the pre-eruptive phase, the gas-thrust phase (i.e. injection of tephra into the atmosphere) and the plume collapse with the propagation of the PDCs.

There is no clear evidence of these different phases in the seismic waveform (Fig. 9.8a). The seismic signal was recorded at the St George's Hill station (MBGH), which is equipped with a broadband, three-component Guralp CGM-40 T seismometer ($T = 30$ s). The signal shows an emergent onset reaching the maximum amplitude after approximately 60 s. Frequency content shows that the main spectral energy is confined in the 1–10 Hz frequency band (Fig. 9.8b). From the seismic ground velocity alone it is, thus, almost impossible to define when the explosion started and to distinguish between different phases of the eruptive dynamics (e.g. De Angelis *et al.* 2007).

The acoustic pressure can be explained as the rate of change of the volumetric outflow (Lighthill 1978). When a volumetric source is expanding, it will produce an equivalent displacement of the overlying atmosphere, and initiate an acoustic wave. An acoustic pressure pulse can be caused by magma accelerating and pushing atmosphere aside at the vent. The duration of an acoustic signal may be indicative of the duration of the gas-thrust phase during the explosive process.

Infrasound recorded 5600 m from the dome clearly marks the explosion onset as a sharp positive pressure peak of 14 Pa, that would give approximately 0.8 bar of excess pressure if reduced to 1 m from the vent (Fig. 9.8c). The acoustic signal therefore allows us to mark the exact time at which the volcanic plume interacts with the atmosphere. Considering a sound speed of 340 m s^{-1}, we adjust the 17:49:19 arrival time at the MVO by 16.47 s, which sets the origin time at 17:49:02. This is consistent with the timing of the thermal image record (Fig. 9.7d, f) used to define the explosion onset.

Dynamics of the eruptive plume

In order to compare the seismic and infrasonic data we adjusted the arrival time of the seismic signal by the distance between the station MBGH and the SHV dome (3880 m). Considering a mean seismic velocity of 2500 m s^{-1} (Luckett *et al.* 2007), this distance converts to a propagation time of 1.55 s. The emergent onset of the seismic ground velocity, once converted for the propagation time, starts at 17:48:49, which is approximately 13 s before the acoustic onset (dashed line Fig. 9.8a–c) and indicates a pre-eruptive dynamics that may be related to the pressurization of the conduit before the explosion onset (Green & Neuberg 2005).

Seismic and infrasound data have been filtered in order to emphasize different components of the eruptive process (Fig. 9.7a, b). The seismic signal converted in displacement and filtered (two poles, zero-phase, non-causal filter) in the 0.03–0.1 Hz frequency range shows a very long period (VLP) component with a frequency of 0.07 Hz. The origin time of this VLP seismic signal (dashed line in Figs 9.7a, b & 9.8a–c) coincides with the onset of the seismic unfiltered ground velocity (Fig. 9.8a, top). This approximately 13 s time delay is reduced to about 10 s when a causal filter is applied (e.g. Patrick *et al.* 2011) to the seismic displacement (grey line in Fig. 9.8a). However, we prefer to use a non-causal filter because it preserves the phase relationship between the original and filtered seismic signals, as shown in Figure 9.7a, b. The correlation between the VLP signal and the eruptive process is more evident when we compare the VLP signal with the infrasound (Fig. 9.7d).

Infrasound is characterized by a low-frequency spectral peak (Fig. 9.8d) at 0.04 Hz (25 s), and it clearly corresponds to the explosion onset with a sharp positive pressure peak lasting around 13 s. This compressive phase is followed by a longer negative coda lasting 29 s.

The maximum amplitude of the VLP seismic displacement (independent of the filter used) coincides (grey marked area in

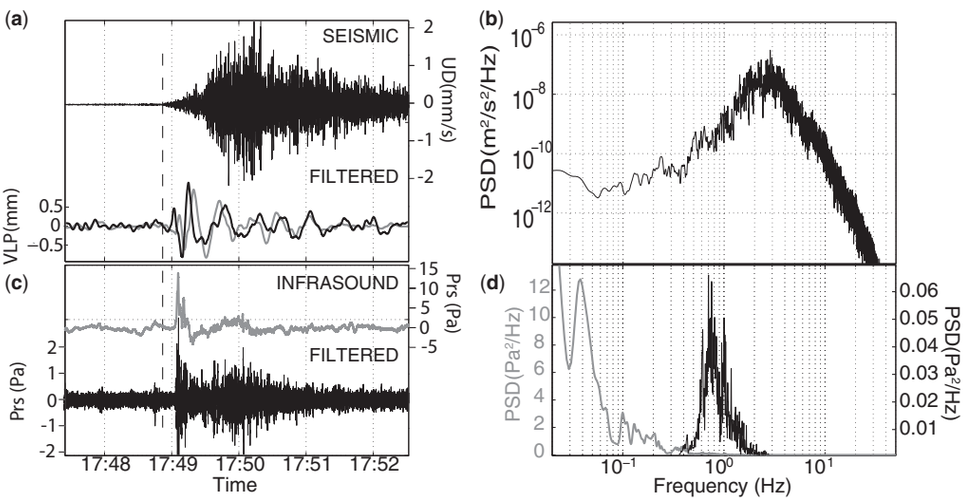

Fig. 9.8. (**a**) (top) Raw seismic ground velocity associated with the Vulcanian explosion of 5 February 2010 and recorded at MBGH shows (**b**) the main spectral energy in the 1–10 Hz frequency range peaked at 3 Hz. (a) (bottom) Seismic displacement, filtered using a causal (grey line) and non-causal (black line) filter between 0.03 and 0.1 Hz, contains a VLP event at 0.07 Hz, which has the maximum amplitude correlated with the eruption onset and the acoustic positive compressive signal (**c**) (top) with a frequency of 0.04 Hz (**d**, grey line). Infrasound filtered in the 0.2–20 Hz range (c, black line) shows a main frequency peak at 0.7 Hz (d, black line) consistent with the acoustic signal generated by PDCs, and coincident with the high-amplitude phase of the seismic ground velocity.

Fig. 9.7) with the positive infrasonic peak, indicating that the VLP seismic signal originated during the initial gas-thrust phase of the explosion. The analysis of the thermal images reveals that the duration of the seismic and infrasonic signals coincides with the duration of the temperature increase (Fig. 9.7f) and with the plume velocity decrease from 170 m s^{-1} to a more constant plume flow of about 27 m s^{-1}. This time corresponds to frame 4 in the thermal sequence of Figure 9.7, and marks the beginning of the column collapse and the onset of the PDCs. Thermal and acoustic data thus suggest that the VLP signal could be generated by a coeruptive source represented by the downwards force of the explosion (Kanamori *et al.* 1984).

Seismic and acoustic signature of PDCs

PDCs at SHV are generally characterized by infrasound in the frequency range of between 0.4 and 2 Hz (Ripepe *et al.* 2010). We have filtered the infrasound above 0.2 Hz to highlight the contribution of the PDC (Fig. 9.7d). However, the explosive dynamics also radiate in this frequency band. The filtered signal shows a sharp infrasonic onset and a pressure peak of approximately 2.5 Pa. This initial signal dies out at the end of the gas-thrust phase but only after the peak of the thermal anomaly (Fig. 9.7f, grey marked area). After that, the infrasound decreases to a minimum amplitude (Fig. 9.7d), which is followed by a second phase of emergent and gradual amplitude increase up to 1 Pa. This second phase represents the infrasound generated by the PDCs, and coincides with the duration and shape of the seismic signal (Fig. 9.7a). This similarity indicates that the seismic signal is dominated by a frequency band above 1 Hz related to PDC activity more than by the explosive process. Moreover, the duration of the high-frequency seismic signal of approximately 7 min coincides with the duration of the infrasound above 1 Hz.

This PDC moving westwards was also detected by thermal camera (Fig. 9.6, frames 6–9), and the propagation vector of the PDC front was calculated by using the previously described thermal image decomposition method (Fig. 9.9a). Front velocities range between 15 and 65 m s^{-1} (Fig. 9.9b), and show a deceleration from 40 to 15 m s^{-1} during approximately the first 15 s followed by a marked acceleration up to 65 m s^{-1} in the following 12 s (Fig. 9.9b). We suggest that this velocity profile reflects two separate PDC events. We propose that an initial small PDC, possibly associated with a minor gravitational collapse of the lava dome, occurred during the initial part of the explosion, and was followed about 15 s later by a larger and more energetic PDC generated by the collapse of the tephra column.

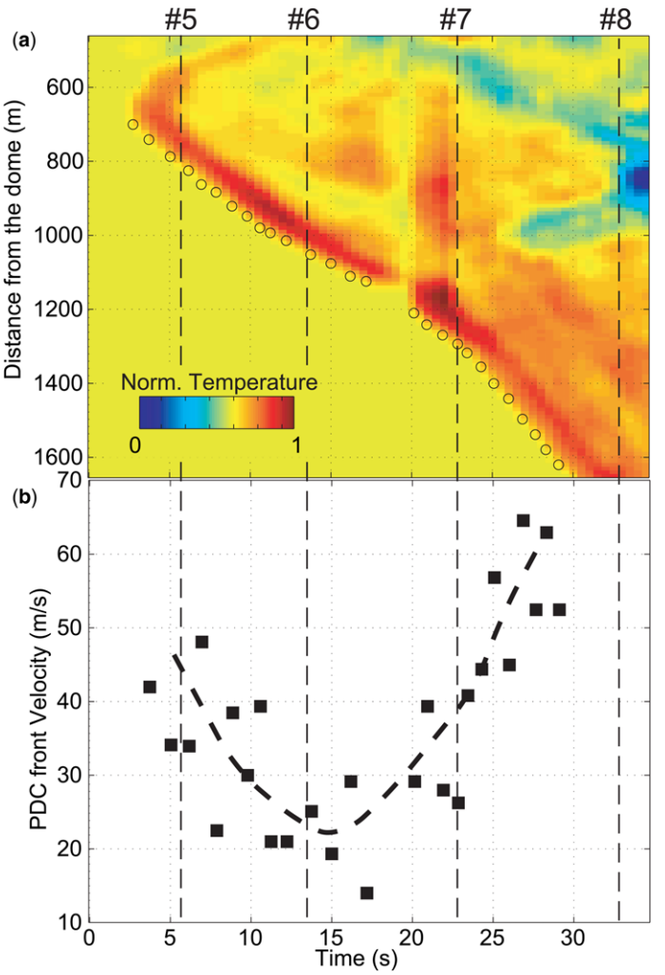

Fig. 9.9. (**a**) Normalized temperature distribution and (**b**) velocity profile associated with the PDC front produced by the 5 February 2010 Vulcanian explosion. Vertical dashed lines and associated numbering are relative to the frames of the thermal images of Figure 9.6. PDC travels westwards with an initial velocity of 40 m s^{-1}, decelerating to 15 m s^{-1} during approximately the first 15 s, and then accelerating up to 65 m s^{-1} in the following 12 s. We interpret this as the evidence of two different PDCs generated by the initial small-dome collapse produced by the explosive dynamics, followed by a larger PDC associated with the ash-plume collapse.

Summary and conclusions

Extrusion of andesite lava at SHV is associated with violent Vulcanian explosions that transport large quantities of tephra to heights of tens of kilometres into the atmosphere. The collapse of tephra columns during explosions and the instability of lava domes are the cause of PDC activity. We have shown how a thermal camera and an infrasonic array provide valuable information that can track and quantify both phenomena. These techniques improve the ability of the MVO to detect and to monitor these phenomena in real time providing the foundation for a reliable risk assessment.

Thermal and infrasonic monitoring techniques allow detection of PDCs, and real-time tracking of their propagation vectors both in terms of flow direction and downhill velocity. In particular, we found that the velocity of the PDCs determined from both thermal and infrasound data processing show comparable values, with an initial peak velocity of the order of approximately 55–75 m s^{-1} decreasing to 20 m s^{-1} within about the first 17 s. Thermal camera 2D images were back-projected onto a DEM, allowing location of the thermal anomaly onto 3D topography. From a monitoring point of view, this improves the ability to visualize the flow run-out in real time, even in poor visibility or at night. However, no infrasound is detected for back-azimuths of less than 127°N. The velocity of the PDC front derived by thermal images indicates that this infrasonic back-azimuth coincides with a constant PDC velocity at approximately 20 m s^{-1} (Fig. 9.5). Although our DEM represents 2008 topography, in which the depression of the 2010 collapse scar is not represented, the 3D thermal images (Fig. 9.3) suggest that the 127°N infrasonic back-azimuth and the deceleration of the PDC front could coincide with a slope change in the topography (Fig. 9.5b, d). Infrasound associated with the PDC seems to be produced by the rapid changes of the PDC front velocity induced by topography.

Infrasound data and thermal camera imagery allow the identification of the onset of Vulcanian explosions and provides constraints on the different phases of the explosive dynamics. This information is more difficult to extract from seismic signals alone, and thus thermal images and infrasound can help in the

interpretation of explosion dynamics. In the case of the 5 February 2010 explosion, thermal camera imagery reveals a temperature increase above the dome lasting for 22 s, which coincides with the onset and the duration of the positive compressive infrasonic signal in the low-frequency band <1 Hz. Furthermore, thermal decomposition of the camera imagery shows a rapid deceleration of the plume velocity from the initial approximately 170 m s^{-1} to a more constant ascent rate of around 27 m s^{-1}.

We attribute this initial eruptive phase as being dominated by the gas-thrust feeding tephra into the atmosphere with a velocity, $U(t)$, which gives an average volumetric discharge rate, $\Phi(t) = \pi R^2 U(t)$, ranging between 3.3×10^4 and 9.2×10^5 m^3 s^{-1}, assuming a vent radius, R, of between 15 and 25 m based on the dimensions of spines extruded from the dome (Watts *et al.* 2002). To estimate the mass flux we need to know the density of the plume. This parameter can be estimated by fall-out distribution and tephra dispersal analysis. Estimations of plume density in Vulcanian explosions with comparable magnitude are given by Ripepe & Harris (2008) and by Pistolesi *et al.* (2011) for the 5 April 2003 and 15 March 2007 Stromboli explosions, respectively. For these explosions, authors estimate a plume density of 6.7 and 13.5 kg m^{-3}, respectively. Using these plume-density values, the mass fluxes of the 5 February 2010 explosion at SHV would be between 0.2×10^6 and 13.3×10^6 kg s^{-1}. Accordingly, the total discharged plume volume of 0.8×10^6–20.2×10^6 m^3 is estimated by integrating the volume flux on the 22 s-long gas-thrust phase, that would give a total discharged mass of 5.4×10^6–272×10^6 kg. This is in agreement with previous estimates using different methods from other Vulcanian eruptions at SHV (Druitt *et al.* 2002; Formenti *et al.* 2003; Komorowski *et al.* 2010; Cole *et al.* 2014).

The seismic signal associated with the gas-thrust phase becomes evident only when filtered below 0.1 Hz in the 0.03–0.1 frequency band. This VLP seismic signal with a frequency of 0.04 Hz seems to be a typical feature of large Vulcanian explosions at SHV, at least in the 2008–2010 period (Cole *et al.* 2014), but not previously reported. Nevertheless, ultra-low-period (ULP >100 s) seismic signals have been recorded by broadband seismometers at SHV (Green & Neuberg 2005) and explained as being related to the pressurization of the upper conduit, presumably by a trapped gas phase.

The fragmentation of overpressurized magmatic foam allows rapid expansion of the magma in the conduit driving material out the vent and into the atmosphere. The ground will react to a change in the upwards momentum induced by the mass discharge with a downwards-orientated counter force (Kanamori *et al.* 1984), which is probably the source of the VLP seismic signal. The correlation with the plume velocity derived by thermal image analysis (Fig. 9.7a, e) seems to support this interpretation.

When eruptive dynamics are no longer able to sustain the column, ejection velocity drops down to 10 m s^{-1} (Fig. 9.7e) and the plume collapses generating PDCs (Fig. 9.6, frames 4–10). Infrasound above 0.2 Hz reveals a high-frequency emergent signal at 0.7 Hz reaching the maximum pressure amplitude approximately 60 s after the eruption onset (Fig. 9.7d). The seismic signal mimics the infrasonic waveform, suggesting that the PDC source is strongly coupled with both the atmosphere and the ground. This indicates that the seismic signal above 1 Hz is not related to the explosive dynamics but is rather caused by the PDC activity. Therefore, the amplitude and duration of the seismic signal (>1 Hz) are not related to the energy and the duration of the explosive process, but, rather, they are related to the amplitude and duration of PDCs that were generated during the plume collapse.

We thank C. 'Pyiko' Williams, N. Fournier and A. Finizola for invaluable support in the field and the scientific discussions on thermal images and acoustic waves. The manuscript has been improved by the critical comments of M. Patrick and J. Johnson.

References

Bookstein, F. L. 1989. Principal warps: thin-plate splines and the decomposition of deformations. *IEEE Transactions on Pattern Analysis and Machine Intelligence*, **11**, 567–585.

Calder, E. S., Cole, P. D. *et al.* 1999. Mobility of pyroclastic flows and surges at the Soufrière Hills Volcano, Montserrat. *Geophysical Research Letters*, **26**, 537–540 http://dx.doi.org/10.1029/1999GL900051

Calder, E. S., Luckett, R., Sparks, R. S. J. & Voight, B. 2002. Mechanisms of lava dome instability and generation of rock-falls and pyroclastic flows at Soufrière Hills Volcano, Montserrat. *In*: Druitt, T. H. & Kokelaar, B. P. (eds) *The Eruption of Soufrière Hills Volcano, Montserrat, from 1995 to 1999*. Geological Society, London, Memoirs, **21**, 173–190.

Cansi, Y. 1995. An automatic seismic event processing for detection and location; the P.M.C.C. method. *Geophysical Research Letters*, **22**, 1021–1024.

Carn, S. A., Watts, R. B., Thompson, G. & Norton, G. E. 2004. Anatomy of a lava dome collapse: the 20 March 2000 event at Soufrière Hills Volcano, Montserrat. *Journal of Volcanology and Geothermal Research*, **131**, 241–264, http://dx.doi.org/10.1016/S0377-0273(03)00364-0

Cole, P. D., Calder, E. S. *et al.* 2002. Deposits from dome-collapse and fountain-collapse pyroclastic flows at Soufrière Hills Volcano, Montserrat. *In*: Druitt, T. H. & Kokelaar, B. P. (eds) *The Eruption of Soufrière Hills Volcano, Montserrat, from 1995 to 1999*. Geological Society London, Memoirs, **21**, 231–262.

Cole, P. D., Smith, P. J., Stinton, A. J., Odbert, H. M., Bernstein, M. L., Komorowski, J. C. & Stewart, R. 2014. Vulcanian explosions at Soufrière Hills Volcano, Montserrat between 2008 and 2010. *In*: Wadge, G., Robertson, R. E. A. & Voight, B. (eds) *The Eruption of Soufrière Hills Volcano, Montserrat from 2000 to 2010*. Geological Society, London, Memoirs, **39**, 93–111, http://dx.doi.org/10.1144/M39.5

De Angelis, S., Bass, V., Hards, V. & Ryan, G. 2007. Seismic characterization of pyroclastic flow activity at Soufrière Hills Volcano, Montserrat, 8 January 2007. *Natural Hazards Earth Systems Science*, **7**, 467–472.

Delle Donne, D. & Ripepe, M. 2012. High-frame rate thermal imagery of Strombolian explosions: implications for explosive and infrasonic source dynamics. *Journal of Geophysical Research*, **117**, B09206, http://dx.doi.org/10.1029/2011JB008987

Druitt, T., Young, S. *et al.* 2002. Episodes of cyclic Vulcanian explosive activity with fountain collapse at Soufrière Hills Volcano, Montserrat. *In*: Druitt, T. & Kokelaar, B. (eds) *The Eruption of Soufrière Hills Volcano, Montserrat, from 1995 to 1999*. Geological Society, London, Memoirs, **21**, 281–306.

Formenti, Y., Druitt, T. H. & Kelfoun, K. 2003. Characterisation of the 1997 Vulcanian explosions of Soufrière Hills Volcano, Montserrat, by video analysis. *Bulletin of Volcanology*, **65**, 587–605, http://dx.doi.org/10.1007/s00445-003-0288-8

Garces, M. A., McNutt, S. R., Hansen, R. A. & Eichelberger, J. C. 2000. Application of wave-theoretical seismoacoustic models to the interpretation of explosion and eruption tremor signals radiated by Pavlov Volcano, Alaska. *Journal of Geophysical Research*, **105**, 3039–3058.

Green, D. N. & Neuberg, J. 2005. Seismic and infrasonic signals associated with an unusual collapse event at the Soufrière Hills volcano, Montserrat. *Geophysical Research Letters*, **32**, L07308, http://dx.doi.org/10.1029/2004GL022265

Hooper, D. M. & Mattioli, G. S. 2001. Kinematic modeling of pyroclastic flows produced by gravitational Dome Collapse at Soufrière Hills Volcano, Montserrat. *Natural Hazards*, **23**, 65–86.

Jolly, A. D., Thompson, G. & Norton, G. E. 2002. Locating pyroclastic flows on Soufrière Hills Volcano, Montserrat, West Indies, using amplitude signals from high dynamic range instruments. *Journal of Volcanology and Geothermal Research*, **118**, 299–317.

Johnson, J. B. 2007. On the relation between infrasound, seismicity, and small pyroclastic explosions at Karymsky Volcano. *Journal of Geophysical Research*, **112**, B08203, http://dx.doi.org/10.1029/2006JB004654

Johnson, J. B. & Ripepe, M. 2011. Volcano Infrasound: a review. *Journal of Volcanology and Geothermal Research*, **206**, 61–69, http://dx.doi.org/10.1016/j.jvolgeores.2011.06.006

Kanamori, H., Given, J. W. & Lay, T. 1984. Analysis of seismic body waves excited by the Mount St. Helens eruption of May 18, 1980. *Journal of Geophysical Research*, **89**, 1856–1866.

Komorowski, J. C., Legendre, Y. *et al.* 2010. Insights into processes and deposits of hazardous vulcanian explosions at Soufrière Hills Volcano during 2008 and 2009 (Montserrat, West Indies). *Geophysical Research Letters*, **37**, L00E19, http://dx.doi.org/10.1029/2010GL042558

Lighthill, M. J. 1978. *Waves in Fluids*. Cambridge University Press, New York.

Luckett, R., Baptie, B. & Ottemoller, L. 2007. Seismic monitoring at Soufrière Hills Volcano, Montserrat. *Seismological Research Letters*, **78**, 192–200, http://dx.doi.org/10.1785/gssrl.78.2.192

Marchetti, E., Ripepe, M., Harris, A. J. L. & Delle Donne, D. 2009. Tracing the differences between Vulcanian and Strombolian explosions using infrasonic and thermal radiation energy. *Earth Planetary Science Letters*, **279**, 273–281, http://dx.doi.org/10.1016/j.epsl.2009.01.004

Nikolkina, I., Zahibo, N., Talipova, T. & Pelinovsky, E. 2011. Pyroclastic flow from Soufrière Hills Volcano, Montserrat: solid block model. *International Journal of Geosciences*, **2**, 326–335.

Oshima, H. & Maekawa, T. 2001. Excitation process of infrasonic waves associated with Merapi-type pyroclastic flow as revealed by a new recording system. *Geophysical Research Letters*, **28**, 1099–1102.

Patrick, M. R. 2007. Dynamics of Strombolian ash plumes from thermal video: motion, morphology, and air entrainment. *Journal of Geophysical Research*, **112**, B06202, http://dx.doi.org/10.1029/2006JB004387

Patrick, M. R., Wilson, D., Fee, D., Orr, T. & Swanson, D. 2011. Shallow degassing events as a trigger for very-long-period seismicity at Kīlauea Volcano, Hawai'i. *Bulletin of Volcanology*, **73**, 1179–1186, http://dx.doi.org/10.1007/s00445-011-0475-y

Pistolesi, M., Delle Donne, D., Pioli, L., Rosi, M. & Ripepe, M. 2011. The 15 March 2007 explosive crisis at Stromboli Volcano, Italy: assessing physical parameters through a multidisciplinary approach. *Journal of Geophysical Research*, **116**, B12206, http://dx.doi.org/10.1029/2011JB008527

Ripepe, M. & Harris, A. J. L. 2008. Dynamics of the 5 April 2003 explosive paroxysm observed at Stromboli by a near-vent thermal, seismic and infrasonic array. *Geophysical Research Letters*, **35**, L07306, http://dx.doi.org/10.1029/2007GL032533

Ripepe, M., Marchetti, E. & Ulivieri, G. 2007. Infrasonic monitoring at Stromboli volcano during the 2003 effusive eruption: insights on the explosive and degassing process of an open conduit system. *Journal of Geophysical Research*, **112**, B09207, http://dx.doi.org/10.1029/2006JB004613

Ripepe, M., De Angelis, S. *et al.* 2009. Tracking Pyroclastic Flows at Soufrière Hills Volcano. *Eos, Transactions of the American Geophysical Union*, **90**, 229–230, http://dx.doi.org/10.1029/2009EO270001

Ripepe, M., De Angelis, S., Lacanna, G. & Voight, B. 2010. Observation of infrasonic and gravity waves at Soufrière Hills Volcano, Montserrat. *Geophysical Research Letters*, **37**, L00E14, http://dx.doi.org/10.1029/2010GL042557

Sparks, R. S. J. & Young, S. R. 2002. The eruption of Soufrière Hills Volcano, Montserrat (1995–1999): overview of scientific results. *In*: Druitt, T. H. & Kokelaar, B. P. (eds) *The Eruption of Soufrière Hills Volcano, Montserrat, from 1995 to 1999*. Geological Society London, Memoirs, **21**, 45–69.

Ulivieri, G., Marchetti, E., Ripepe, M., Chiambretti, I., De Rosa, G. & Segor, V. 2011. Monitoring snow avalanches in Northwestern Italian Alps using an infrasound array. *Cold Regions Science and Technology*, **69**, 177–183.

Vergniolle, S. & Caplan-Auerbach, J. 2006. Basaltic thermals and sub-Plinian plumes: constraints from acoustic measurements at Shishaldin volcano, Alaska. *Bulletin of Volcanology*, **68**, 611–630.

Wadge, G., Jackson, P., Bower, S. M., Woods, W. & Calder, E. 1998. Computer simulations of pyroclastic flows from dome collapse. *Geophysical Research Letters*, **25**, 3677–3680.

Watts, R. B., Herd, R. A., Sparks, R. S. J. & Young, S. R. 2002. Growth patterns and emplacement of the andesite lava dome at Soufrière Hills Volcano, Montserrat. *In*: Druitt, T. H. & Kokelaar, B. P. (eds) *The Eruption of Soufrière Hills Volcano, Montserrat, from 1995 to 1999*. Geological Society London, Memoirs, **21**, 115–152.

Wilson, L. 1980. Relationships between pressure, volatile content and ejecta velocity in three types of volcanic explosion. *Journal of Volcanology and Geothermal Research*, **8**, 297–313.

Yamasato, H. 1997. Quantitative analysis of pyroclastic flows using infrasonic and seismic data at Unzen volcano, Japan. *Journal of Physics of the Earth*, **45**, 397–416.

Yokoo, A. & Iguchi, M. 2010. Using infrasound waves from eruption video to explain ground deformation preceding the eruption of Suwanosejima volcano, Japan. *Journal of Volcanology and Geothermal Research*, **196**, 287–294.

Young, S. R., Sparks, R. S. J., Aspinall, W. P., Lynch, L. L., Miller, A. D., Robertson, R. E. A. & Shepherd, J. B. 1998. Overview of the eruption of Soufrière Hills volcano, Montserrat, July 18 1995 to December 1997. *Geophysical Research Letters*, **25**, 3389–3392.